

# IN-SITU ANALYSIS OF REVERTED AUSTENITE IN SUPERMARTENSITIC STAINLESS STEEL WELD DEPOSITS

S. Zappa<sup>1,2</sup>, J.J. Hoyos<sup>3</sup>, L. Tufaro<sup>4</sup>, H. Svoboda<sup>2,3</sup>

<sup>1</sup>Universidad Nacional de Lomas de Zamora, Facultad de Ingeniería, Buenos Aires, Argentina

<sup>2</sup>Consejo Nacional de Investigaciones Científicas y Tecnológicas, CABA, Argentina

<sup>3</sup>Universidad de Buenos Aires, Facultad de Ingeniería, Departamento de Ingeniería Mecánica, Buenos Aires, Argentina

<sup>4</sup>Instituto Nacional de Tecnología Industrial, Buenos Aires, Argentina

## ABSTRACT

To increase the toughness, ductility and resistance to localized corrosion in supermartensitic stainless steel weld deposits, suitable post weld heat treatments are required, since these properties are controlled by the microstructure. In this sense, the austenite transformation or stability is a key issue. The aim of this work is to analyze “in-situ” the evolution of austenite during the heating, maintenance and cooling in post weld inter-critical heat treatment in a supermartensitic stainless steel weld deposit, by means of a thermomechanical simulator integrated on a synchrotron X-ray diffraction line. All weld metal coupon was welded with a semi-automatic process. On samples extracted from the welded coupon, dilatometry measurements were performed at different heating rates (1, 10 and 100 °C/s) in the thermomechanical simulator, in order to determine the critical transformation temperatures. To study phase transformation during the apply post weld heat treatment cycles (heating to 665 °C at 1 °C/s, maintenance during 15 min and cooling to room temperature at 2 °C/s), in-situ synchrotron X-ray diffraction measurements were carried in the facilities of National Laboratory Synchrotron Light (Campinas, Brasil). The microstructural evolution was discussed in terms of volumetric phase fractions, micro-deformation and crystallite size. The techniques used make it possible to detect the critical transformation temperatures, phase transformations and their kinetics, monitoring particularly the austenite evolution during the post weld heat treatments cycle. At the inter-critical temperature 71% of austenite was formed, after 15 min of permanence. Finally, at room temperature 29% of stable reverted austenite was obtained.

**Keywords:** Dilatometry; Critical Temperatures; Synchrotron X-Ray Diffraction; Post Weld Heat Treatment; Austenite Stability.

## 1.- INTRODUCTION

Supermartensitic stainless steels (*SMSS*) are developed from classic martensitic stainless steels (11–14% Cr), reducing *C* content to enhance weldability and corrosion resistance and adding *Ni* to promote a free ferrite structure and *Mo*, which also improves corrosion resistance [1]. In recent years, this steel has been used with greater intensity in flow lines for transporting unprocessed fluid in the oil and gas industry, replacing classic martensitic and duplex stainless steels, due to the appropriate combination of weldability, toughness, corrosion resistance and the ease of performing heat treatments, at a comparatively lower price [2, 3]. Generally, these materials are an economical alternative against uncoated carbon steels, carbon steel used without inhibitors or duplex stainless steels in some environments [3]. Furthermore, their relatively lower cost makes them an attractive option as a substitute for more expensive duplex and super duplex stainless steels, and their use in offshore deep water tubing applications has increased significantly in recent years [4].

*SMSS* exhibits the following typical mechanical properties: 25-32 RC hardness, 650-750 MPa of 0.2% offset yield strength, 880-950 MPa tensile strength, elongation at rupture of up to 20%, and impact energy of up to 100 J [5]. These properties strongly depend on the microstructure at room temperature, which is usually depending on the heat treatment history and composition [6].

In the present alloy grade, delta ferrite is the first solidifying phase (1480 to 1460 °C), which partially or completely transforms to austenite during cooling (1380 to 1180 °C). The main austenite to martensite transformation occurs at lower temperatures (230 to 190 °C) [7]. In this sentences, *SMSS* also consist of martensite and variable amount of austenite (up to 30%) and ferrite (up to 10%), with different morphologies [1]. The presence of the ferrite phase can cause severe reduction of toughness and ductility. Further, it can locally interrupt the passivation layer through *Cr*-depletion in martensite and formation of *Cr* carbides near ferrite, which leads to degradation of the corrosion

resistance [8]. When retained, it is only possible to dissolve ferrite by extensive heat treatment, which is uneconomical and can lead to undesired grain growth [8].

The high toughness of the steel is usually achieved when the tempering temperature is close to austenite start temperature ( $A_s$ ), owing to the existence of amounts of finely distributed austenite along the martensite interlath boundaries and prior austenite grain boundaries [5, 9, 10]. Inappropriate heat treatment may cause important changes in microstructure and serious decrease in mechanical property value [9]. In this sentences, the content of retained austenite gradually increases with intercritical temperature up to maximum value. As the intercritical temperature continues to rise, the content of retained austenite gradually decreases [6, 9].

The austenite start and finish temperature ( $A_s - A_f$ ) transformation range during welding and *PWHT* is strongly dependent on the heating rate. As the heating rate increases, the ( $A_s - A_f$ ) transformation range increases [7]. The initial critical temperature of austenite into martensite transformation during the cooling ( $M_s$ ) in *SMSS* welding deposit is in the order of 130 °C [11].

Post weld heat treatments (*PWHT*) is usually recommended for welded joints of these steels in order to temper the martensite, thus improving the toughness and ductility. Because of the increased *Ni* content, the  $A_s$  temperature is usually lower than 600 °C, and correspondingly lower than the typical tempering range for martensitic steels (650 – 750 °C). Tempering above the  $A_s$  will result in reformation of some austenite and subsequent formation of “fresh” martensite upon cooling. The presence of untempered martensite and potential for a high fraction of retained austenite following *PWHT* can compromise the mechanical properties of the weldment [7].

The retained austenite formed during the heating process and retained to room temperature is related to the additional alloying elements (*Ni* and *Mo*) [9]. The *PWHT* leads to formation of reverted austenite in a finely dispersed lamellar morphology on grain boundaries of lath martensite. These places present high defect density, which can provide the energy of austenite nucleation and the quick diffusion access for *Ni* [12]. This is accompanied by diffusion of austenite stabilizing elements into austenite, which stabilize this phase to room temperature [8]. In this way, through a diffusional mechanism, the austenite produced during the tempering is enriched in elements such as *N*, *C* and *Ni*. This enrichment will determine the stability of austenite formed during the treatment. If tempering is carried out at temperatures slightly above  $A_s$ , the enriched austenite will be stable at room temperature. On the other hand, if the treatment is performed at temperatures well above or well below  $A_s$ , the austenite will lose chemical enrichment and, consequently, its stability. Thus, the martensitic transformation is easily induced owing to the decrease of thermal instability of austenite [12-14]. Since the good mechanical properties of the alloy depend on this stabilization of reverted austenite, it is vital to control the compositional homogeneity of the initial martensitic microstructure prior to tempering [8].

The reverted austenite will not transform into martensite even at very low temperatures. However, once plastic deformation occurs, the reverted austenite will absorb the deformation work and transform to martensite partially. Thereby, the plasticity and toughness of material at low temperatures can be enhanced [12].

The aim of this work is to analyze “in-situ” the evolution of austenite during the heating, maintenance and cooling in post weld inter-critical heat treatment in a *SMSS* weld deposit, by means of a thermomechanical simulator (*TMS*) integrated on a Synchrotron X-Ray Diffraction (*S - XRD*) line.

## 2.- EXPERIMENTAL PROCEDURE

### 2.1.- Materials

An all-weld metal (*AWM*) coupon was welded according to the AWS A5.22 [15] standard. Metal Cored Arc Welding (*MCAW*) process was employed, with *SMSS* tubular filler wire of 1.2 mm diameter, using an *Ar* + 5%*He* gas protection, with a flow rate of 18 L/min. The welding was done in a flat position, the electrode to piece distance was approximately 20 mm, and preheat and inter-pass temperatures were 100 °C. Table 1 shows the welding parameters used.

Table 1. Welding parameters used

Coupon	Tension	Current	Weld. Speed	Heat input
	[V]	[A]	[mm/s]	[kJ/mm]
<i>SMSS</i>	29	298	5	1.7

Figure 1.A shows a macrograph of a cross section of the weld deposit, where different zones can be observed: base metal plates, buttered area and the central area of *AWM* zone. Transversal specimens for dilatometry and phase transformations studies were extracted centered on the *AWM* zone, according to the scheme of the Figure 1.B. Their thickness was 2 mm. This zone is free from dilution with the adjacent sheets, so that the chemical composition is associated to the filler material. To assure the position of the sample, electro discharge machining (*EDM*) wire cutting was used with a 0.2 mm diameter *Mo* wire.

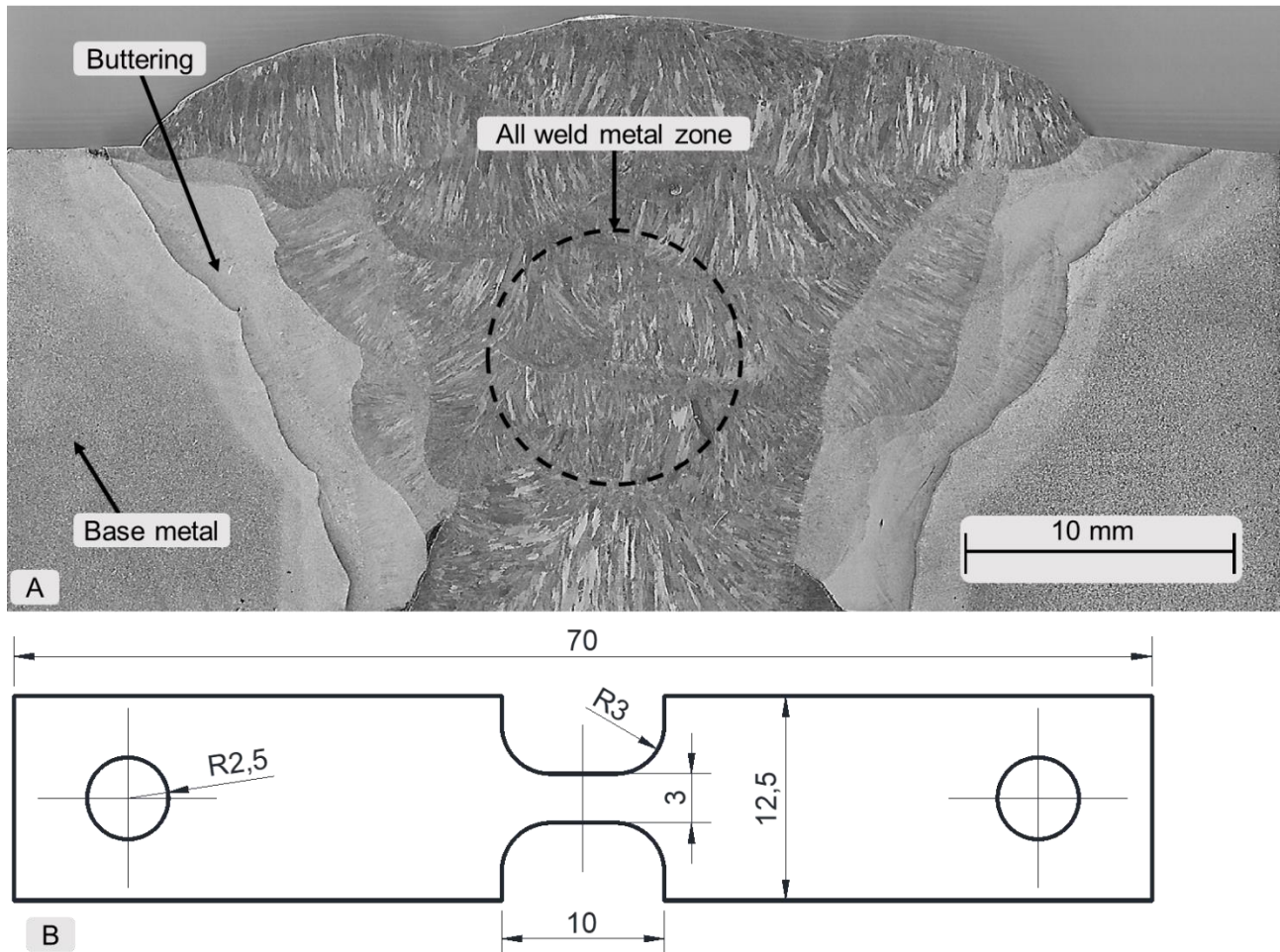


Figure 1.- A: All weld metal coupon for *SMSS*; B: Dimensions of the specimens for dilatometry and phase transformations studies

The chemical composition at the *AWM* zone was measured by optical emission spectrometry, except for the *C*, *O*, *N* and *S* contents that were analyzed by combustion techniques. Initial microstructure and fraction of phases were also analyzed by means of scanning electron microscopy (*SEM*) and X-Ray Diffraction (*XRD*).

## 2.2.- Dilatometry

Dilatometry tests were carried out in order to determine the critical transformation temperatures (*A<sub>s</sub>* and *A<sub>f</sub>*) at three different Heating Rates (*HR*) according to Table 2.

Table 2.- Parameters for dilatometry studies

Coupon	Heating Rate	Temperature	Time hold	Cooling rate
	[°C/s]	[°C]	[s]	[°C/s]
<i>SMSS</i>	1	1000	60	20
	10	1000	60	20
	100	1000	60	20

Samples shown in Figure 1.B were used. A thermocouple type K was welded at the center of the calibrated length of them. These tests were carried out at a Gleeble<sup>TM</sup> 3S50. For each case, curves dilatation vs. temperature were obtained, from which  $A_s$ ,  $A_f$  and  $M_s$  temperatures were determined.

### 2.3.- Intercritical tempering

The critical transformation temperatures experimentally determined by dilatometry ( $A_s$  and  $A_f$ ) were used to define the  $PWHT$  temperature at 665 °C. Such intercritical tempering temperature was established as  $A_s + 40$  °C, since the highest reverted austenite contents are reached at this temperature [2]. For this condition, the heating and cooling rates were 1 and 2 °C/s, respectively under vacuum atmosphere.

To study the kinetics of austenite transformation during the intercritical  $PWHT$  (heating, holding and cooling) in-situ  $S - XRD$  measurements were carried out. The experiments were carried out using a beam of light with an energy of 12 keV and a wavelength of 0.10332 nm. The diffracted intensity was measured using two solid state linear detectors (Mythen of 1080 pixels each one), which simultaneously measured a 20 ° angular region around the center of the specimens. It was placed in a fixed position and inclined at 15 ° in relation to the incident beam. The heat treatment was carried out in a vacuum atmosphere (10<sup>-1</sup> Pa). The obtained data during the different stages of the  $PWHT$ , were recorded with an angle 2θ of 28 to 49 ° (since it is the maximum amplitude of the detectors), identifying in this way the austenite peaks corresponding to planes {111}, {200} and {220} and martensite / ferrite {110} and {200}, with an acquisition time of 3.15 seconds at room temperature. As the temperature increases, the number of identified peaks of each phase increases. This means that every 3.15 seconds, a  $XRD$  spectrum with information about the microstructure evolution during heating, permanence or cooling is obtained. In addition, to get a more detailed information, complete scans within a 2θ range from 28 to 88 °, with a scan time of 210 sec, were performed in constant temperature stages.

From the  $XRD$  spectra measured, the volume fractions  $x_i$  of the particular phases were estimated from the integrated intensity  $I_i$  and the theoretical intensity  $R_i$  of each diffraction peak, according to Equations 1 to 3, respectively [16, 17].

$$x_i = \frac{\frac{1}{N} \sum_{j=1}^N \left( \frac{I_{i,j}^{hkl}}{R_{i,j}^{hkl}} \right)}{\sum_i \left( \frac{1}{N} \sum_{j=1}^N \left( \frac{I_{i,j}^{hkl}}{R_{i,j}^{hkl}} \right) \right)} \quad \text{Equation 1}$$

$$R^{hkl} = \frac{\rho^{hkl} |F^{hkl}|^2 \left( e^{-\left(1 + \frac{\sin \omega}{\sin(2\theta - \omega)} + 2M(\theta)\right)} \right)}{v_i^2 (4 \sin^2 \theta \cos \theta)} \quad \text{Equation 2}$$

$$M(\theta) = \frac{6 h^2 T}{m k \Phi^2} \left( \varphi(x) + \frac{x}{4} \right) \left( \frac{\sin(\theta)}{\lambda} \right)^2 \quad \text{Equation 3}$$

Where  $\rho^{hkl}$  is the plane multiplicity factor,  $F^{hkl}$  is the plane structure factor,  $v_i$  is the volume of the unit cell,  $\theta$  the Bragg angle,  $\omega$  the angle of incident beam (around 15 °),  $M(\theta)$  the Debye-Waller factor,  $h$  the Planck's constant (6.63×10<sup>-34</sup> m<sup>2</sup>Kg/s),  $T$  the absolute temperature,  $m$  the mass of the vibrating atom,  $k$  the Boltzmann's constant (1.38×10<sup>-23</sup> m<sup>2</sup>Kgs<sup>-2</sup>K<sup>-1</sup>),  $\Phi$  the Debye characteristic temperature of steel,  $x$  the ration between the Debye and steel temperatures,  $\lambda$  the wavelength in angstroms (1.033 Angstroms),  $\varphi(x)$  the Debye function.

The average crystallite size and lattice microstrain of each phase were estimated using the Williamson – Hall method [18, 19], according to Equation 4. In this method, the scan spectra were employees ( $AWC$  at 25 °C, Holding at 665 °C and intercritical condition at 25 °C). For martensite, the following families of planes were used: {110}; {200}; {211}; {220}; {222}; {321}. On the other hand, for austenite, the following families of planes were used: {111}; {200}; {220}; {311}; {222}; {331}; {420}.

$$\frac{(\beta \cos \theta)}{\lambda} = \left( \frac{1}{D} \right) + 4 \eta \left( \frac{\sin \theta}{\lambda} \right) \quad \text{Equation 4}$$

Where  $D$  is the crystallite size,  $\eta$  the lattice microstrain, and  $\beta$  is the Full Width at Half Maximum corrected ( $FWHM$ ). The  $D$  and  $\eta$  were respectively obtained from the intercept and the slope of

$\beta \cos\theta / \lambda$  plotted against  $4 \sin\theta / \lambda$ . The instrument broadening was calculated according to Equation 5, reported by Caglioti [20, 21].

$$FWHM = (0.004289 \tan^2 \theta + 0.000548 \tan \theta + 0.001102)^{1/2} \quad \text{Equation 5}$$

Nevertheless, the crystallite size of the austenite is not reported since the values are negative, and consequently, do not have physical meaning [18]. In this sentences, the average crystallite size ( $D$ ) of each phase was estimated from the Scherrer Equation, according to Equation 6. It is worth noting that this equation lead to an underestimation of the Crystallite Size because it does not consider the effects of the lattice strain in the peak broadening.

$$D = \left( \frac{\lambda}{\beta \cos\theta} \right) \quad \text{Equation 6}$$

Figure 2 shows an image corresponding to the Gleeble 3S50 equipment linked to the X-ray diffraction line and the imposed intercritical treatment cycle.

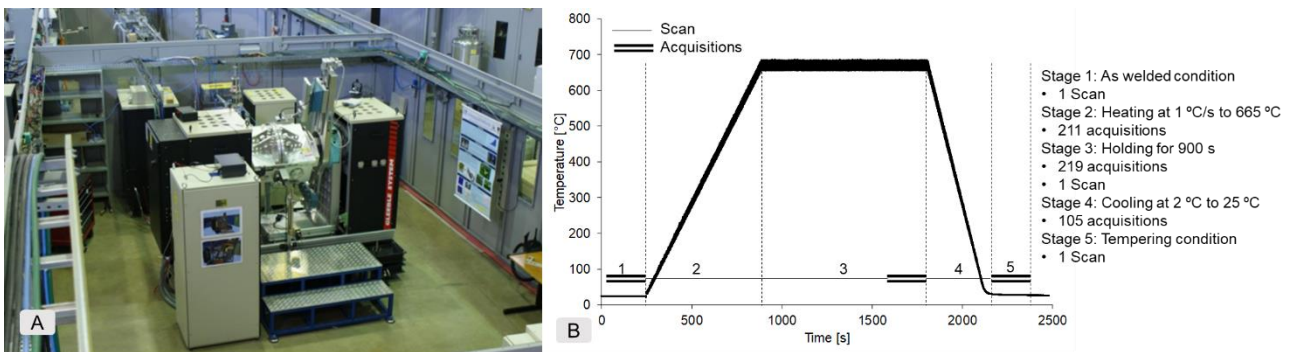


Figure 2.- A: Gleeble 3S50 equipment linked to the X-ray diffraction line; B: intercritical treatment cycle

### 3. RESULTS AND DISCUSSION

#### 3.1 Chemical composition

Table 3 shows the chemical composition measured from the SMSS steel weld metal. The obtained values are according with the specified for this material [13].  $O$  and  $N$  are also in contents usually observed.

Table 3.- Chemical composition of the weld deposit

$C$	$Mn$	$Si$	$S$	$P$	$Cr$	$Ni$	$Mo$	$Cu$	$V$	$Nb$	$O$	$N$
[%wt]	[ppm]	[ppm]										
0.012	1.76	0.44	0.013	0.015	12.13	6.27	2.69	0.49	0.09	0.01	390	50

In martensitic stainless steel with high  $Ni$  content,  $A_s$  can be around 550 °C [22]. In the literature there were proposed different equations to estimate  $A_s$ , Equation 6 and  $M_s$ , Equation 7 [13, 22, 23].

$$A_s = 850 - 1500(C + N) - 50Ni - 25Mn + 25Si + 25Mo + 20(Cr - 10) \quad \text{Equation 6}$$

$$M_s = 540 - 497C - 6.3Mn - 36.3Ni - 10Cr - 46.6Mo \quad \text{Equation 7}$$

According to Equation 6 and 7,  $A_s$  temperature should be 588 °C and the  $M_s$  temperature 49 °C, respectively, for the SMSS weld deposit analyzed in this work. However, these equations are for reference only, since they do not consider heating rate, cooling rate, initial microstructure, segregations, etc.

#### 3.2 Dilatometry

Figure 3 shows the dilatometry curves for different heating rate studies, A: 1 °C/s, B: 10 °C/s and C: 100 °C/s, measure and filtered data. In these curves, the obtained initial and final critical temperatures of transformation of martensite into austenite,  $A_s$  and  $A_f$ , during heating can be

identify. Furthermore,  $M_s$  can also be observed. In this sense, the  $M_f$  (final critical temperature of transformation of austenite into martensite) could not be identified graphically, because it is under room temperature. Table 4 shows the values of critical temperatures experimentally determined.

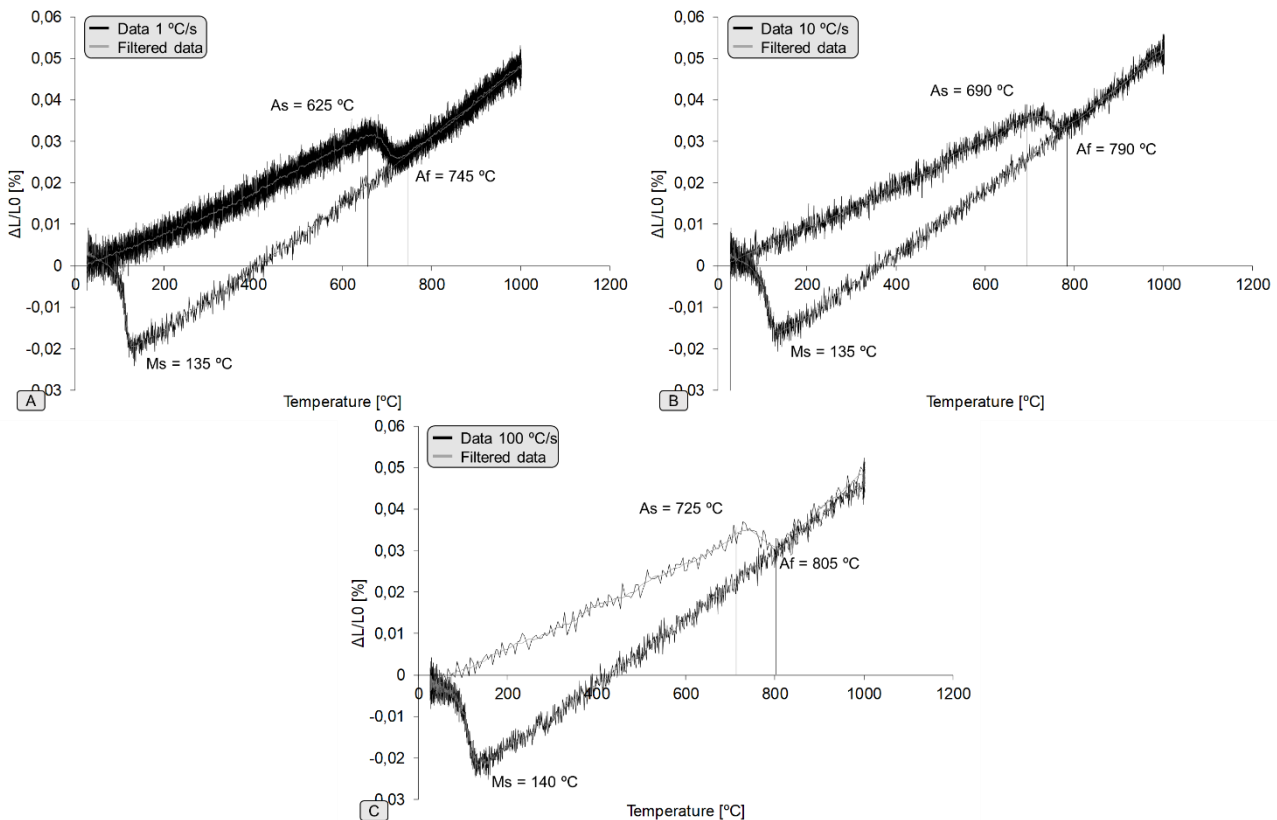


Figure 3.- Dilatomety curves for different heating rates. Filtered and real data

Table 4.- Critical temperatures determined by dilatometry

$HR$	$A_s$	$A_f$	$A_s - A_f$	$M_s$
[°C/s]	[°C]	[°C]	[°C]	[°C]
1	625	745	120	135
10	690	790	100	135
100	725	805	80	140

The initial and final critical temperature of transformation of martensite into austenite showed dependence with the heating rate in the analyzed welded deposit, as it was previously reported for other materials [24]. As the heating rate increased from 1 to 100 °C/s, the  $A_s$  temperature increased. The same behavior was found for the  $A_f$  temperature, but more attenuated. The characteristic transformation temperatures are shifted to higher temperatures with increasing heating rate, which is a well-known effect due to the thermally activated character of the transformation [25]. The range of transformation of martensite into austenite ( $A_f - A_s$ ) decreases as the  $HR$  increases. These results show the importance of controlling the  $HR$  during the application of heat treatments, especially in those materials that have a narrow range of critical temperatures, such as supermartensitic stainless steel [7, 22].

### 3.3.- Stage 1: As welded condition

In Figure 4 it can be seen a SEM image and XRD pattern of the SMSS weld metal in AWC. Martensite with a low content of ferrite can be observed in the Figure 4.A [11]. Also, peaks corresponding to austenite and martensite/ferrite can be identify in the XRD pattern of the Figure 4.B. A predominantly martensitic matrix, with the presence of 9 % delta ferrite (in its different morphologies) and 5 % retained austenite was observer. The presence of ferrite and austenite is due to the incomplete transformation into austenite and martensite, respectively, in solid state during cooling. As mentioned above, the ferrite and retained austenite content, control the final properties in opposite directions.

A higher content of ferrite and retained austenite decreases and increases, respectively, the toughness and ductility of the weld deposits [13].

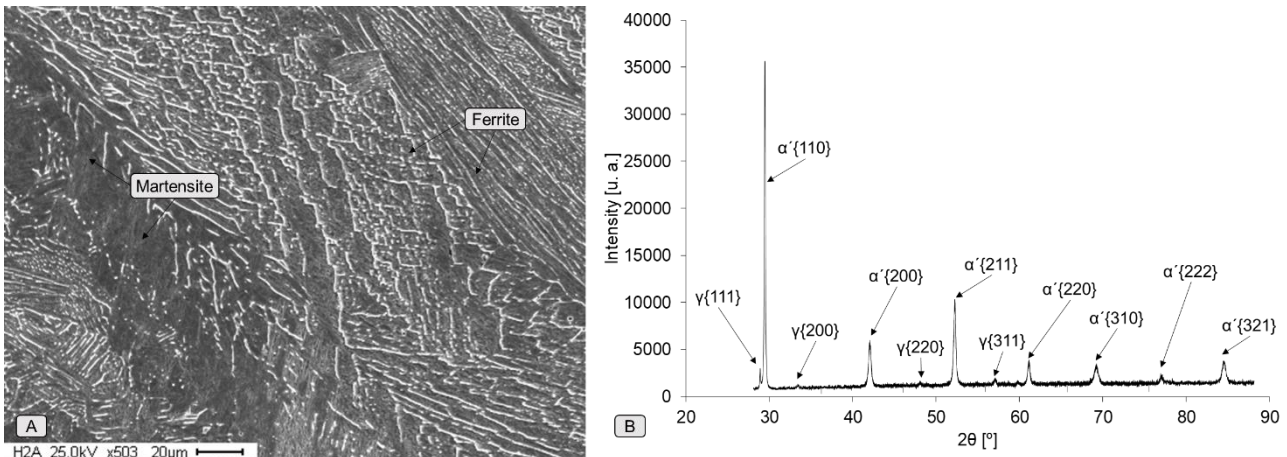


Figure 4.- Microstructure in as welded condition. A: SEM; B: XRD

### 3.4.- Stage 2: Heating at 1 °C/s to 665 °C

Figure 5 shows the evolution of the main austenite peak {111} during heating. A shift of all austenite and martensite peaks towards the left can be observed, with lower angles, associated with phase dilation phenomena and the increase in the inter-planar distance generated by temperature [26]. In this sense, the shift of austenite is greater than that of martensite, associated with the higher coefficient of linear expansion of the austenite [27]. In addition, from 621 °C the growth of the austenite peaks and the decrease of the peaks corresponding to martensite were observed. This evolution corresponds to the transformation of martensite into austenite, thus identifying the lower critical temperature  $A_s$ .

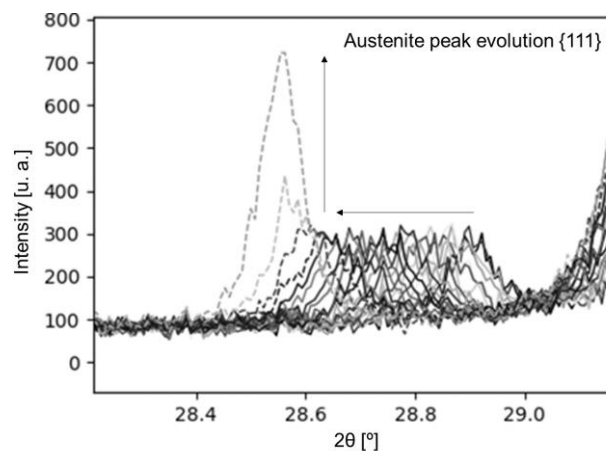


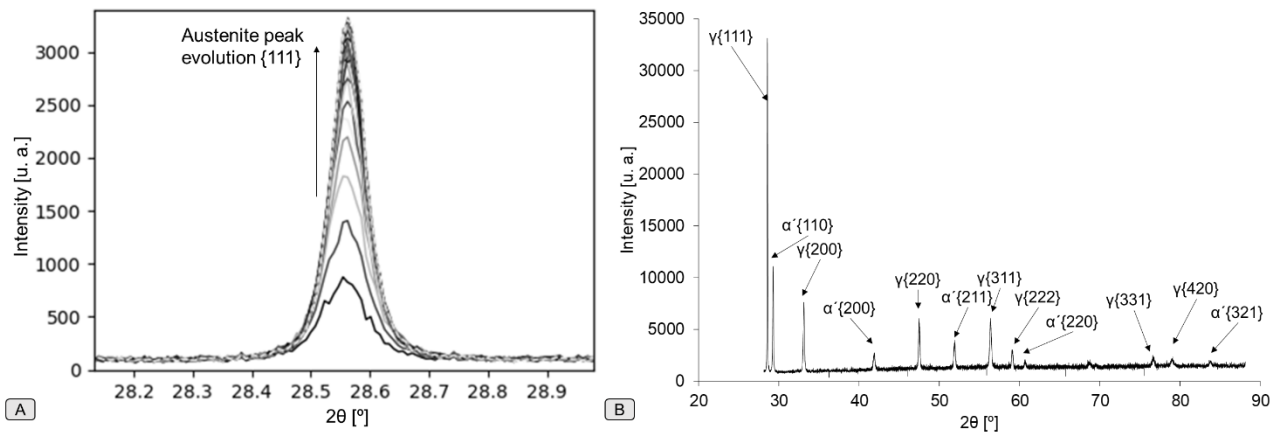
Figure 5.- Shift and growth of the main austenite peak {111} during heating

It is known for the SMSS steel that  $Ni$  is crucial for stabilizing the austenite at room temperature, because austenite is enriched in  $Ni$  during heating and tempering. Since  $Ni$  lowers the temperature range over which austenite is stable in the 13Cr6Ni2Mo SMSS,  $Ni$  rich zones are transformed first to austenite during heating, followed by  $Ni$  depleted zones. Whereby the  $Ni$  rich regions transform to austenite first, due to their lower  $A_s$  temperature [27]. In this sense, other authors [28] report that a higher rate of transformation of martensite into austenite is achieved for SMSS steels with higher  $Ni$  contents.

### 3.4.- Stage 3: Holding for 900 s

Figure 6.A shows the superposition of various diffraction spectra during the first 11.5 minutes of permanence at 665 °C. It was observed that once the intercritical tempering temperature is reached, austenite grows rapidly during the first 514 seconds (8.5 minutes). After this time, there is no growth of austenite, which remains constant until the end of the tempering time. In this instance, no peak

shifting is observed, since the temperature was kept constant. Figure 6.B shows the XRD spectrum of the sample for this condition. In the final instance of intercritical tempering, the austenite content was approximately 71%.

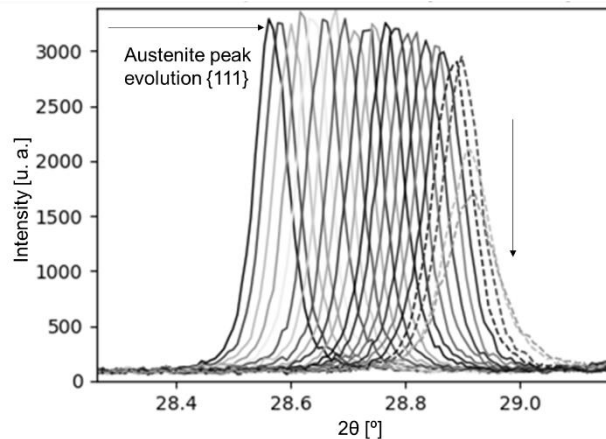


Figur 6.- A: Growth of the main austenite peak {111} during maintenance; B: XRD

In this steel, this transformation behavior from martensite to austenite at constant temperature, was previously reported [25]. In dilatometry tests, the change in relative length during holding is greater for higher heating rates. These observations again imply the process being diffusional [25].

### 3.5.- Stage 4: Cooling at 2 °C/s to 25 °C

Figure 7 shows the overlap of various diffraction spectra as it was cooled from 665 °C to room temperature. A shift of all austenite and martensite peaks towards the right, greater angles, can be observed, associated with contraction phenomena of the phases and the decrease in the interplanar distance generated by temperature [26]. Starting at 150 °C, a decrease in austenite peaks and an increase in martensite peaks were observed. This evolution corresponds to the transformation of austenite into martensite  $M_s$ . As the literature indicates [27], during cooling the transformation of austenite into martensite occurs by a shear process.



Figur 7.- Shift and decrease of the main austenite peak {111} during cooling

### 3.6.- Stage 5: Tempering condition

Figure 8 shows an electron microscopy image and the X-ray diffraction spectrum of the SMSS weld deposit in the tempering condition. A microstructure consisting of a martensitic matrix with a low ferrite content in its different morphologies can be observed, as indicated by the literature [11] for these materials, since tempering does not alter the ferrite content. The estimated austenite content for this last condition was 29%. In this sense, the final microstructure for this condition consisted of 20% tempered martensite (the martensite that did not transform into austenite during tempering), 9% ferrite (since intercritical tempering does not alter this phase), 29% of reverted austenite (the

austenite that remained stable after cooling the tempering) and 42% of fresh martensite (that new martensite that comes from the transformation of austenite during the cooling of the tempering).

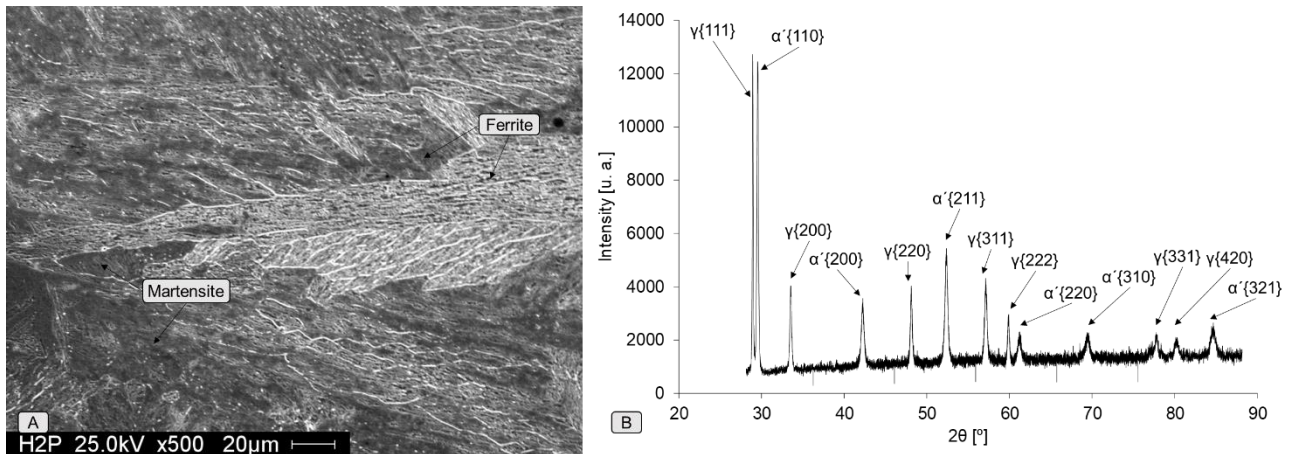


Figure 8.- Microstructure in tempering condition. A: SEM; B: XRD

The literature [29] reported the increase of toughness with tempering treatments and attributed to the increase of reverted austenite and the TRIP effect. Also, the experimental results confirmed that the reverted austenite had a beneficial effect on the intergranular corrosion of the martensitic stainless steel via the following two ways. Firstly, the formation of reverted austenite at the Cr-depleted regions reduced the number of nucleation sites for intergranular corrosion. Secondly, the reverted austenite was always distributed along the martensite lath boundaries, which prevented the propagation of intergranular corrosion [30].

### 3.7.- Nucleation, growth and stability of austenite

There are three main mechanisms reported in the literature [31] for the generation of nanometric size austenite:

1. Generation of allotriomorphic austenite (with irregular faces) coherent at the interface (with K-S orientation), housed between martensite lath, aided by a strong segregation of gamma-gene elements.
2. Growth of a previously existing retained or reverted austenite.
3. Austenite nucleation aided by the precipitation of carbides that act as heterogeneous nucleation sites.

In this sense, the austenite generation mechanism accepted in the literature [31] is mainly associated with the segregation of austenite stabilizing elements at the edges between martensite lath, followed by austenite nucleation and growth, mainly controlled by the local equilibrium partition of  $Ni$  at the tempering temperature.

According to the literature [25, 27, 32, 33], the mechanism that explains the stability of reverted austenite at room temperature is associated with chemical and morphological issues. During heating, before reaching the temperature  $A_s$ , the progressive segregation of  $Ni$ ,  $Mn$ ,  $C$  and  $N$  is generated, mainly at the edge of the grain, associated with the tempering of the martensite. In this sense, said segregation of elements generates a change in the volume of the elemental cell of martensite [34]. However, this phenomenon does not participate in the generation of austenite, as indicated by the literature [31]. Once the  $A_s$  temperature is reached, the austenite content grows, enriching itself in gamma-gene elements (mainly  $Ni$  and  $Mn$ ), as mentioned above. In this sense, the stability of the austenite particles depends on the intercritical tempering temperature, which generates a greater or less enrichment of  $Ni$  for low or high intercritical temperatures, respectively. Austenite particles with more than 8%  $Ni$  in solution will be retained after cooling [33]. According to the literature [33], the stability of austenite is divided into three regions, depending on the temperature of the tempering heat treatment:

1. Total stability (temperatures close to  $A_s$ ).
2. Partial stability (temperatures between  $A_s$  and  $A_f$ ).
3. Instability (temperatures close to or above  $A_f$ ).

In our case, the heat treatment used in this work corresponds to stage 2, since not all the austenite generated at high temperature remained stable at room temperature. In this sense, during cooling part of the reverted austenite is transformed into fresh martensite (saturated in  $C$ ). According to the literature [35], the stable reverted austenite and the recently created fresh martensite have the same morphology, but different chemical compositions.

Figure 9 shows schematics of the microstructure for the conditions studied in the present work: AWC at 25 °C; final stage of maintenance at 665 °C; condition after intercritical temper cooling at 25 °C.

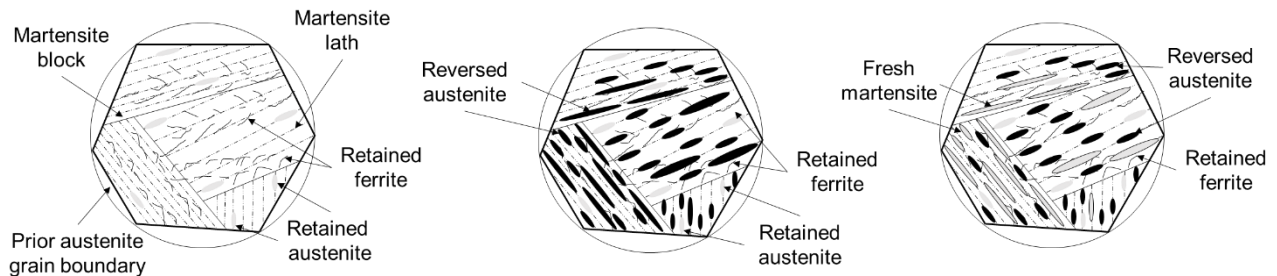


Figure 9.- Schemes of the microstructure in the different stages of heat treatment

Figure 10.A shows the intensity map, while 10.B the evolution of the austenite content during the heating, holding and cooling stage of the intercritical tempering cycle. In this sense, in Figure 10 it can be seen that austenite grows from 621 °C. Once the tempering temperature is reached, the austenite content continues to grow (for 8.5 minutes) up to 71%. During cooling, below 150 °C, austenite begins to transform into a martensite. Finally, after intercritical tempering, the microstructure is made up of 20% tempered martensite, 9% delta ferrite, 29% reverted austenite and 42% fresh martensite.

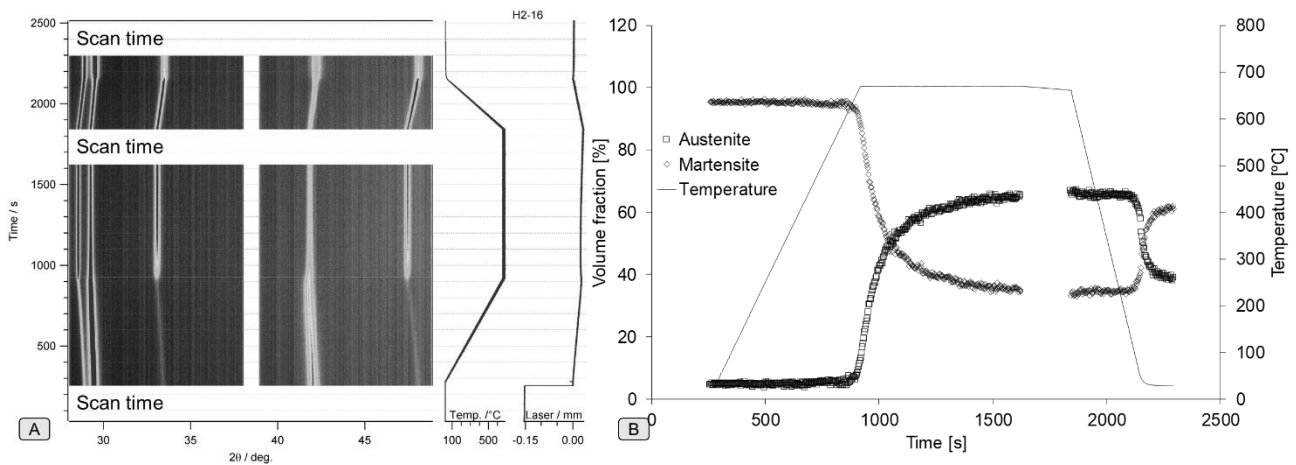


Figure 10.- A: Intensity map; B: Austenite content evolution

According to the literature [36], coherent diffraction domains (crystallites) are expected to get larger as tempering proceeds. Consequently, the changes in crystallite size are mirrored on peak narrowing. Since both lattice distortion (microstrain) and crystallite size can be followed by peak broadening analysis, it is imperative to separate both influences from the observed peak width. In this regards, Figure 11 shows the Williamson-Hall method, where the microstrain and crystallite size of martensite and austenite can be determined in AWC at 25 °C, holding at 665 °C and intercritical condition at 25 °C (scan spectra were employees). Table 5 shows the values obtained for the lattice microstrain and crystallite size associated with the slope and the inverse of the intercept, respectively. It can be seen that the thermal cycle does not generate large changes both in microstrain as well as in crystallite size. However, the following can be observed: First, the microstrain in retained austenite is greater than in martensite. In addition, for both phases the microstrain decreased during maintenance up to 665 °C (45.3% for austenite and 22.5% for martensite). Finally, after tempering at room temperature, the microstrain for both phases increases. In this sense, it is observed that the microstrain of the martensite in the tempering condition is higher than that of the martensite in the welded condition, indicating a greater lattice distortion.

As mentioned in the experimental procedure, it was not possible to determine the crystallite size for austenite, since for this phase the intercept is negative. On the other hand, the crystallite size for martensite increased from 590 to 1022 Angstroms, associated with the increase in temperature [36]. Finally, the crystallite size after intercritical tempering at room temperature was 429 Angstroms.

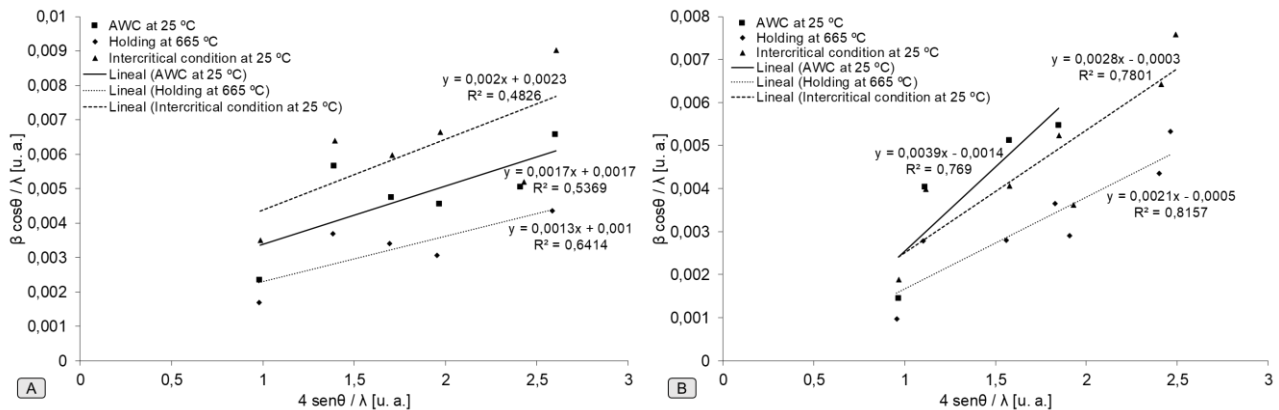


Figure 11.- Williamson-Hall method for A: martensite and B: austenite

Table 5.- Williamson-Hall method for martensite and austenite

Phase	Condition	Microstrain	Crystallite Size
		[u. a.]	[Angstroms]
Martensite	AWC at 25 °C	0,00169286	590
	Holding at 665 °C	0,00131384	1022
	Intercritical condition at 25 °C	0,00204919	429
Austenite	AWC at 25 °C	0,00390318	-
	Holding at 665 °C	0,00213308	-
	Intercritical condition at 25 °C	0,00284966	-

Additionally, the crystal size was determined by the Scherrer equation, for the martensite and the austenite according to Figure 12. In particular, the calculations were performed during the heating up to 665 °C, holding at 665 °C and cooling up to 25 °C.

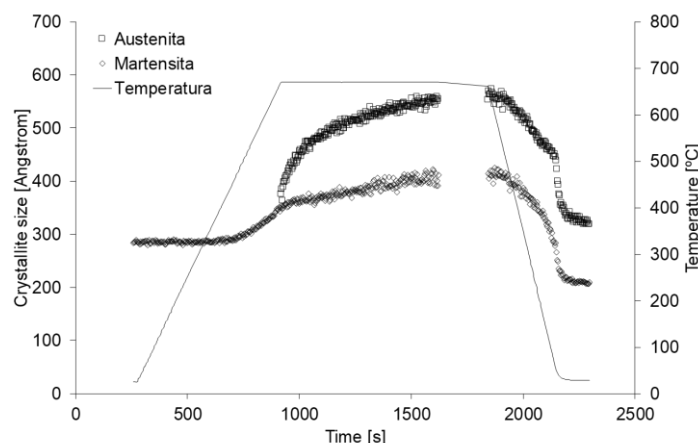


Figure 12.- Scherrer equation for martensite and austenite

According to Figure 12, it can be observed that the crystallite size increases as the temperature increases until reaching 665 °C in both phases. In the same way, during the holding at 665 °C, the crystallite size continues to grow, but in a more accentuated way in austenite. In this sense, the increase in the crystallite size generates an increase in the grain boundary and the lattice parameter. This increase is associated with an increase in temperature [36]. However, the segregation or enrichment of certain chemical elements also alter the lattice parameter. According to the literature [27] Ni would decrease the lattice parameter and hence the obtained lattice parameter should be smaller. Other elements that also enrich austenite during heating, such as Cr and Mn, generate an

increase in the lattice parameter. Therefore, the effects of  $Ni$  and other elements on the austenite lattice parameter, which are enriched in austenite, are overlapping. Finally, during cooling from 665 °C, the crystallite size decreases to its original size.

#### 4. CONCLUSIONES

The lower and upper critical temperatures  $A_s$  and  $A_f$  respectively, showed dependence with the heating rate. As the heating rate increased from 1 to 100 °C/sec, the  $A_s$  temperature increased from 625 to 725 °C.

The microstructure in  $AWC$  consisted of martensitic matrix, 9% ferrite and 5% retained austenite. During heating to the tempering temperature, the phases present expand. For 1 °C/s, above 621 °C, martensite begins to transform into austenite up to 665 °C. In this instance, the reverted austenite is formed by nucleation and growth mechanism. The preferential nucleation sites could be associated with areas segregated in gamma-gene elements and retained austenite. Once the tempering temperature is reached and, until the first 8.5 minutes, the martensite continues to transform into austenite in an isothermal manner. In the final stage of the holding at 665 °C, the reverted austenite content was in the order of 71%. During cooling, when passing 150 °C, said austenite begins to transform into fresh martensite. In this way, after intercritical tempering, the microstructure consisted of a high content of tempered martensite, retained ferrite, fresh martensite, and a high content of reverted austenite. Both Williamson-Hall and Scherrer show similar results for both phases in microstrain and crystallite size: there were no significant variations during the thermal cycle.

If the initial microstructure had been a chemically homogeneous structure and without retained austenite (without preferential nucleation sites), the behavior of the reverted austenite would be another, an interesting situation to study in a future work.

#### 5. ACKNOWLEDGMENT

The authors wish to thank CONARCO-ESAB for the donation of the filler metals, Air Liquide for the donation of the shielding gases, LNLS (Laboratório Nacional de Luz Síncrotron) for the facilities of the tests, Leonardo Wu of LNNano (Laboratório Nacional de Nanotecnologia) for the assistance, at the FI-UNLZ, INTECIN and INTI for financial support.

#### 6. REFERENCIAS:

1. M, C., L. K, and S. P, *Characterization and Optimization of TIG welded supermartensitic stainless steel using TOPSIS*. Materials Today: Proceedings, 2017. **4**(2017): p. 1662–1669.
2. Sebastián, Z., S. Estela, and S. Hernán, *Effects of Welding Procedure on Corrosion Resistance and Hydrogen Embrittlement of Supermartensitic Stainless Steel Deposits*. JOURNAL OF IRON AND STEEL RESEARCH, INTERNATIONAL, 2013. **20**(12): p. 124-132.
3. Srinivasan, P.B., S.W. Sharkawy, and W. Dietzel, *Environmental Cracking Behavior of Submerged Arc-Welded Supermartensitic Stainless Steel Weldments*. Journal of Materials Engineering and Performance, 2004. **13**(2): p. 232 - 236.
4. Pieta, G., et al., *Evaluation of the Fracture Toughness of a SMSS Subjected to Common Heat Treatment Cycles in an Aggressive Environment*. Journal of Materials Engineering and Performance, 2010. **19**(9): p. 1318 - 1324.
5. Rodrigues, C.A.D., et al., *Effect of phosphorus content on the mechanical, microstructure and corrosion properties of supermartensitic stainless steel*. Materials Science and Engineering: A, 2016. **650**(5): p. 75-83.
6. Lian, Y., et al., *Effect of 0.2 and 0.5% Ti on the microstructure and mechanical properties of 13Cr supermartensitic stainless steel*. Journal of Materials Engineering and Performance, 2015. **24**(11): p. 4253 - 4259.
7. Lippold, J.C. and B.T. Alexandrov. *Phase transformation during welding and postweld heat treatment of 12Cr-6,5Ni-2,5Mo supermartensitic stainless steel*. in *Stainless Steel Word 2004*. 2004. Netherlands.
8. Niessen, F., N.S. Tiedje, and J. Hald, *Kinetics modeling of delta-ferrite formation and retainment during casting of supermartensitic stainless steel*. Materials and Design, 2017. **118**: p. 138-145.

9. De-ning, Z., et al., *Influence of Tempering Process on Mechanical Properties of 00Cr13Ni4Mo Supermartensitic Stainless Steel*. JOURNAL OF IRON AND STEEL RESEARCH, INTERNATIONAL, 2010. **17**(8): p. 50-54.
10. Solheim, K.G., et al., *The role of retained austenite in hydrogen embrittlement of supermartensitic stainless steel*. Engineering Failure Analysis, 2013. **34**: p. 140–149.
11. Svoboda, S.Z.H., et al., *Improving Supermartensitic Stainless Steel Weld Metal Toughness*. WELDING JOURNAL, 2012. **91**(March): p. 83s-90s.
12. Yu-rong, L., et al., *Effect of Heat Treatment on Microstructure and Property of Cr13 Super Martensitic Stainless Steel*. JOURNAL OF IRON AND STEEL RESEARCH, INTERNATIONAL, 2011. **18**(11): p. 60-66.
13. Zappa, S., H. Svoboda, and E. Surian, *Effect of Post-weld Heat Treatment on the Mechanical Properties of Supermartensitic Stainless Steel Deposit*. Journal of Materials Engineering and Performance, 2017. **26**(2): p. 514-521.
14. ZOU, D.-n., et al., *Influence of Heat Treatment Temperature on Microstructure and Property of 0 0Cr 1 3 Ni 5 Mo 2 Supermartensitic Stainless Steel*. JOURNAL OF IRON AND STEEL RESEARCH, INTERNATIONAL, 2014. **21**(3): p. 3 6 4 - 3 6 8 .
15. A5.22, A., *Specification for Stainless Steel Electrodes for Flux Cored Arc Welding and Stainless Steel Flux Cored Rods for Gas Tungsten Arc Welding*. AWS Standards, American Welding Society 2012.
16. Cullity, B.D. and S.R. Stock, *Elements of X Ray Diffraction*. 3rd Edition ed. 2001.
17. Ivanov, I.V., et al., *Rearrangements of dislocations during continuous heating of deformed  $\beta$ -TiNb alloy observed by in-situ synchrotron X-ray diffraction*. Materials Characterization, 2020. **166**: p. 110403.
18. WILLIAMSON, G.K. and W.H. HALL, *X-RAY LINE BROADENING FROM FILED ALUMINIUM AND WOLFRAM*. Acta Metallurgica 1953. **1**: p. 22-31.
19. Lanfredi, S., et al., *Structural characterization and Curie temperature determination of a sodium strontium niobate ferroelectric nanostructured powder*. Journal of Solid State Chemistry, 2011. **184**: p. 990–1000.
20. Carvalho, A.M.G., et al., *X-ray powder diffraction at the XRD1 beamline at LNLS* Journal of Synchrotron Radiation 2016. **23**(6): p. 1501-1506.
21. CAGLIOTI, G., A. PAOLETTI, and F.P. RICCI, *CHOICE OF COLLIMATORS FOR A CRYSTAL SPECTROMETER FOR NEUTRON DIFFRACTION*. Nucl. Instrum., 1958. **3**: p. 223-228.
22. Gooch, T.G., P. Woollin, and A.G. Haynes, *Welding metallurgy of low carbon 13% chromium martensitic steel*, in *Supermartensitic Stainless Steel '99*, B.W. Institute, Editor. 1999: Belgian. p. 188-195.
23. Wu, W., et al., *THE RELATIONSHIP BETWEEN ALLOYING ELEMENTS AND RETAINED AUSTENITE IN MARTENSITIC STAINLESS STEEL WELDS*. Scripta Materiala, 2000. **42**: p. 1071–1076.
24. Niessen, F., et al., *Kinetics analysis of two-stage austenitization in supermartensitic stainless steel*. Materials and Design, 2017. **116**: p. 8-15.
25. SIETSMA, A.B.L.Z.P.F.M.J., *Austenite Formation from Martensite in a 13Cr6Ni2Mo Supermartensitic Stainless Steel*. METALLURGICAL AND MATERIALS TRANSACTIONS A, 2016. **47A**: p. 1996-2009.
26. MARÍN, J.V.R., *IDENTIFICACIÓN Y CUANTIFICACIÓN DE FASES EN ACERO INOXIDABLE ASTM A743 GRADO CA6NM MEDIANTE LA TÉCNICA DE DIFRACCIÓN DE RAYOS X*, in *FACULTAD DE MINAS - ESCUELA DE INGENIERÍA DE MATERIALES*. 2009, UNIVERSIDAD NACIONAL DE COLOMBIA: Medellín, Colombia. p. 66.
27. Bojack, A., et al., *In-situ determination of austenite and martensite formation in 13Cr6Ni2Mo supermartensitic stainless steel*. M A T E R I A L S C H A R A C T E R I Z A T I O N, 2012. **71**: p. 7 7 – 8 6 .
28. Rodrigues, C.A.D., et al., *The Influence of Ni Content on the Weldability, Mechanical, and Pitting Corrosion Properties of a High-Nickel-Bearing Supermartensitic Stainless Steel*. Journal of Materials Engineering and Performance, 2021. **30**(4): p. 3044–3053.
29. Tavares, S.S.M., et al., *GTAW of 12% Supermartensitic Stainless Steel Using 625 Nickel Alloy as Filler Metal*. Materials Research, 2021. **24**(5): p. 1-7.

30. Man, C., et al., *Beneficial effect of reversed austenite on the intergranular corrosion resistance of martensitic stainless steel*. Corrosion Science, 2019. **151**: p. 108-121.
31. Escobar, J.D., et al., *Compositional analysis on the reverted austenite and tempered martensite in a Ti-stabilized supermartensitic stainless steel: segregation, partitioning and carbide precipitation*. Materials & Design, 2017. **15**: p. 95-105.
32. Niessen, F., et al., *Formation and stabilization of reversed austenite in supermartensitic stainless steel*, in *24th International Federation for Heat Treatment and Surface Engineering Congress 2017*: Nice, France.
33. Escobar, J.D., et al., *Austenite reversion kinetics and stability during tempering of a Ti-stabilized supermartensitic stainless steel: Correlative in situ synchrotron x-ray diffraction and dilatometry*. Acta Materialia, 2017. **138**: p. 92-99.
34. Niessen, F., et al., *In-situ analysis of redistribution of carbon and nitrogen during tempering of low interstitial martensitic stainless steel*. Scripta Materialia, 2018. **154**: p. 216-219.
35. Escobar, J.D., et al., *Meta-equilibrium transition microstructure for maximum austenite stability and minimum hardness in a Ti-stabilized supermartensitic stainless steel*. Materials and Design, 2018. **156**: p. 609–621.
36. Filho, I.R.S., et al., *Austenite reversion in AISI 201 austenitic stainless steel evaluated via in situ synchrotron X-ray diffraction during slow continuous annealing*. Materials Science & Engineering A, 2019. **755**: p. 267-277.